

High spatial resolution collinear chiral sum-frequency generation microscopy

Ziheng Ji,^{a,b} Wentao Yu,^{b,c} Dashan Dong,^{b,d} Hong Yang,^{b,d,e} Kaihui Liu,^b Yun-Feng Xiao,^{b,d,e} Qihuang Gong,^{b,d,e} Qinghai Song,^{a,d,*} and Kebin Shi^{b,d,e,*}

^aHarbin Institute of Technology (Shenzhen), School of Science, Ministry of Industry and Information Technology Key Lab of Micro-Nano Optoelectronic Information System, Shenzhen, China

^bPeking University, School of Physics, State Key Laboratory for Mesoscopic Physics and Frontiers Science Center for Nano-Optoelectronics, Beijing, China

^cNanjing University of Science and Technology, Institute of Interdisciplinary Physical Sciences, School of Science, Nanjing, China

^dShanxi University, Collaborative Innovation Center of Extreme Optics, Taiyuan, China

^ePeking University Yangtze Delta Institute of Optoelectronics, Nantong, China

Abstract. Chiral sum-frequency generation (SFG) has proven to be a versatile spectroscopic and imaging tool for probing chirality. However, due to polarization restriction, the conventional chiral SFG microscopes have mostly adopted noncollinear beam configurations, which only partially cover the aperture of microscope and strongly spoil the spatial resolution. In this study, we report the first experimental demonstration of collinear chiral SFG microscopy, which fundamentally supports diffraction-limited resolution. This advancement is attributed to the collinear focus of a radially polarized vectorial beam and a linearly polarized (LP) beam. The tightly focused vectorial beam has a very strong longitudinal component, which interacts with the LP beam and produces the chiral SFG. The collinear configuration can utilize the full aperture and thus push the spatial resolution close to the diffraction limit. This technique can potentially boost the understanding of chiral systems.

Keywords: chiral sum-frequency generation; radially polarized beam; nonlinear optical microscopy.

Received Jan. 17, 2024; accepted for publication Jan. 19, 2024; published online Mar. 8, 2024.

© The Authors. Published by SPIE and CLP under a Creative Commons Attribution 4.0 International License. Distribution or reproduction of this work in whole or in part requires full attribution of the original publication, including its DOI.

[DOI: [10.1117/1.APN.3.2.026006](https://doi.org/10.1117/1.APN.3.2.026006)]

1 Introduction

Chirality refers to a system that is distinguishable from its mirror image.¹ This property can influence both molecular interaction and light–matter interactions, which not only has importance in chemistry, biology, and pharmacology, but also leads to a chiral optical response that enables the optical characterization of the chiral system.² Various techniques have been developed to detect and understand chiral materials. Chiral sum-frequency generation (SFG)^{3–5} is a prominent example. It has higher sensitivity than circular dichroism² and is not limited to interfaces like chiral second-harmonic generation.⁶ Owing to the symmetry-determined nonlinear susceptibility^{2,4} and the resonant enhancement,^{7,8} chiral SFG provides both the chiral selectivity and the chemical bond selectivity. Over the past few decades, chiral SFG has proven

to be a powerful spectroscopic tool⁹ for studying chiral liquids³ and proteins embedded in lipid membranes.^{10,11} Later by adapting into microscope system, chiral SFG microscopy was invented,¹² which has found applications in cellular imaging¹³ and data storage.¹⁴

Despite its continuous successes, the spatial resolution of chiral SFG microscopy is strongly constrained. In principle, chiral SFG is a three-wave mixing process that occurs through the chiral elements of the quadratic susceptibility tensor, $\chi_{ijk}^{(2)} (i \neq j \neq k)$.^{3,4} All participating electric fields must be mutually perpendicular to each other, which makes it necessary to employ noncollinear beam geometry to satisfy this orthogonal polarization restriction.² However, the noncollinear approach only utilizes partial aperture of the objective lens in an off-axis manner, thereby strongly hindering the spatial resolution. To improve the spatial resolution, it is favorable to align the excitation beams collinearly and cover the full aperture of the objective lens. This is possible for achiral SFG microscopy,^{15,16} which

*Address all correspondence to Kebin Shi, kebinshi@pku.edu.cn, Qinghai Song, qinghai.song@hit.edu.cn

does not have an orthogonal polarization restriction. In contrast, for chiral SFG, the collinear configuration has only been theoretically proposed by considering the small longitudinal electric field component derived from focused Gaussian beam as excitation,¹⁷ but it has not been realized due to the low efficiency of longitudinal polarization conversion. To date, a chiral SFG microscope with diffraction-limited resolution is still absent in experiments. Here we report the first experimental demonstration of high-resolution chiral SFG microscopy that has access to a full numerical aperture (NA).

2 Working Principle

Generally, chiral SFG excitation requires a visible beam with fixed wavelength and an IR beam with tunable wavelength. The induced chiral SFG polarization is perpendicular to both of the excitation electric fields and can be expressed as

$$\vec{P}(\omega_1 + \omega_2) = \epsilon_0 \chi_{ijk}^{(2)} \vec{E}_1(\omega_1) \vec{E}_2(\omega_2), \quad (i \neq j \neq k). \quad (1)$$

In conventional studies, two incident beams are usually linearly polarized (LP). To produce propagating chiral SFG, the two incident beams must be horizontally separated and focused with a noncollinear configuration [Fig. 1(a)]. In such a case, only a partial NA of the objective lens is utilized, which strongly restricts spatial resolution. Meanwhile, the direction of chiral SFG signals is strongly dependent on the alignment of incident beams, posing additional difficulties in integrating with other optical systems.

The above challenge can be tackled with the recently developed structured light, e.g., vectorial beam.^{18–20} In contrast to linear polarization, a radially polarized (RP) vectorial beam can produce a strong longitudinal polarization at the focus. According to Eq. (1), a collinear configuration is apparently feasible. We employ the configuration shown in Fig. 1(b), where the vectorial beam is collinearly focused with an LP beam. Here, the second beam can fully utilize the NA of the objective lens,

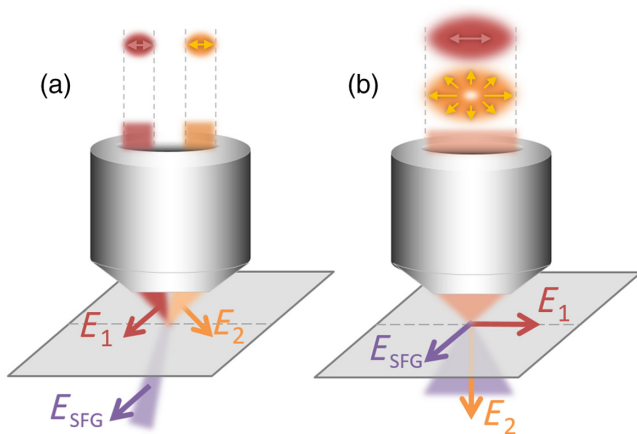


Fig. 1 Schematics of chiral SFG microscope. (a) Conventional noncollinear setup, which uses two separated linear-polarized beams, has sub-optimum NA. (b) Collinear setup, which uses linearly and radially polarized beams, can utilize the full NA with rotational symmetry. The top insets show the cross-sections of the excitation beams and the polarization arrangement at the objective aperture. E_{SFG} , E_1 and E_2 are the electric fields of the SFG signal and the two incident beams, respectively.

resulting in several intrinsic advantages, such as co-directional propagation for easy integration, higher spatial resolution, and higher sensitivity at both the interface and bulk regions.

3 Results and Discussion

3.1 Simulation of Spatial Resolution

To illustrate the advantage of a collinear system, we calculate the three-dimensional intensity distribution of the foci and the chiral SFG point spread function (PSF). The excitations are delivered by focusing two laser beams with wavelengths of 520 and 820 nm using a 1.4 NA objective lens. For the collinear modality [Fig. 2(a)], the foci are two well-overlapped and diffraction-limited spots [Fig. 2(b)], resulting in a tight SFG PSF elongated along the optical axis [Fig. 2(c)]. A direct comparison with the noncollinear modality [Fig. 2(d)] reveals that the foci [Fig. 2(e)] are much larger than the diffraction limit and tilted in different directions, leading to a larger and tilted SFG PSF [Fig. 2(f)]. In potential applications, the visible beam's wavelength can be tuned to scan the SFG wavelength across an electronic resonance. Figure 3 shows the dependence of the PSF full width at half-maximum (FWHM) on an SFG wavelength. Since the noncollinear PSF is tilted, to ensure a fair comparison, the FWHM of the noncollinear PSF is measured along the major, median, and minor axis of the ellipsoid. The quantitative result shows that the transverse resolution of collinear modality is 1.7 times that of noncollinear modality.

3.2 Simulation of Phase Matching

The collinear configuration offers inherent advantages in phase matching and the efficiency of chiral SFG as well. Using Green's function formulation,²¹ which calculates the signal's dependence on sample size, we evaluated the phase-matching condition of collinear and noncollinear modality. Specifically, a reference sphere is centered at the focus and its diameter D varies from 0.1 to 4 μm . For each diameter, we calculated the far-field SFG signal distribution generated by the $\vec{P}^{NL}(\omega_1 + \omega_2)$ within the sphere, and then integrated the far-field signal within a collection NA of 0.5 (to match the NA of the UV objective lens used in the experiment). We studied the integrated signal as a function of D for two scenarios: focusing on the interface between a chiral liquid and an achiral medium [Fig. 4(a)], and focusing inside the bulk of a uniform chiral liquid [Fig. 4(b)]. Figure 4 reveals that the collinear modality produces a higher signal compared to that of the noncollinear modality. Furthermore, as the sample size increases, collinear modality generates accumulating signals when focused on the interface and retains a higher proportion of signals when focused in the bulk. This indicates a better phase-matching condition compared to noncollinear modality, as the signal experiences less destructive interference during generation and propagation. In addition, the faster initial increasing trend is also evidence of a tighter PSF. The energy flux of incident beams is normalized to allow for a fair comparison. At the focal plane, 47.2% of the RP beam energy flux can be converted into the longitudinal polarization component.

This approach holds great potential for use in mid-infrared wavelengths for vibrational resonance measurement, despite the challenge posed by the smaller NA of the reflective objective lens. The corresponding results and analysis for the foci, signal PSF, and phase-matching evaluation are presented in the [Supplementary Material](#).

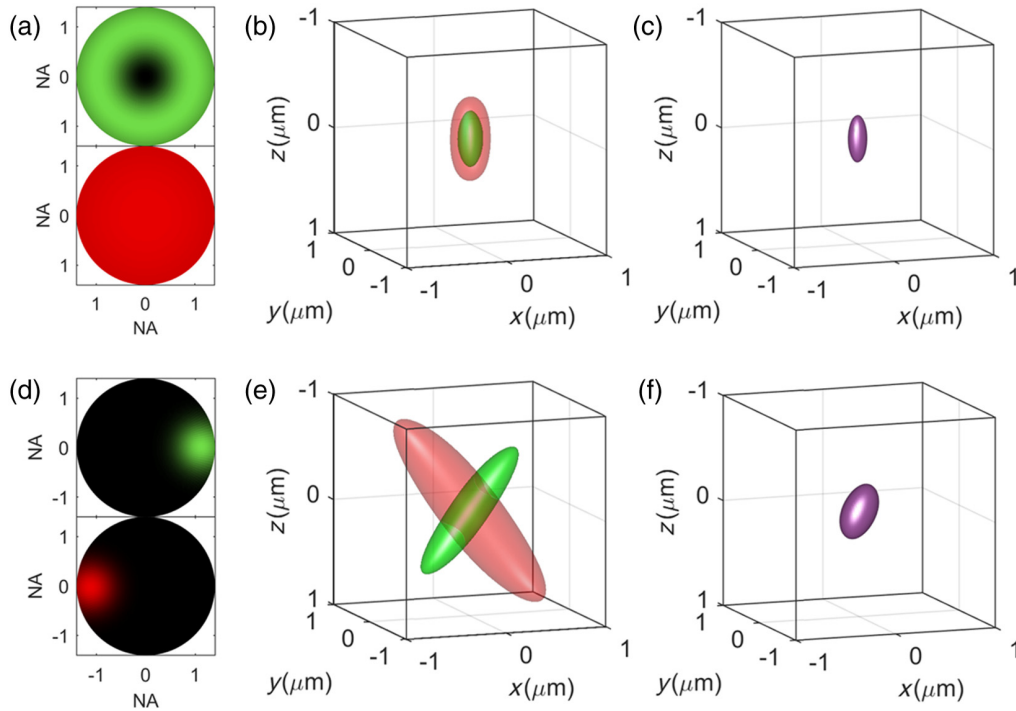


Fig. 2 Numerical simulation of the foci and the chiral SFG PSF. The first row depicts collinear modality: (a) laser intensity at the objective lens pupil, (b) foci, and (c) chiral SFG PSF. The second row depicts noncollinear modality: (d) laser intensity at the objective lens pupil, (e) foci, and (f) chiral SFG PSF. The colors green, red, and purple are used to represent wavelengths of 520, 820, and 318.2 nm, respectively.

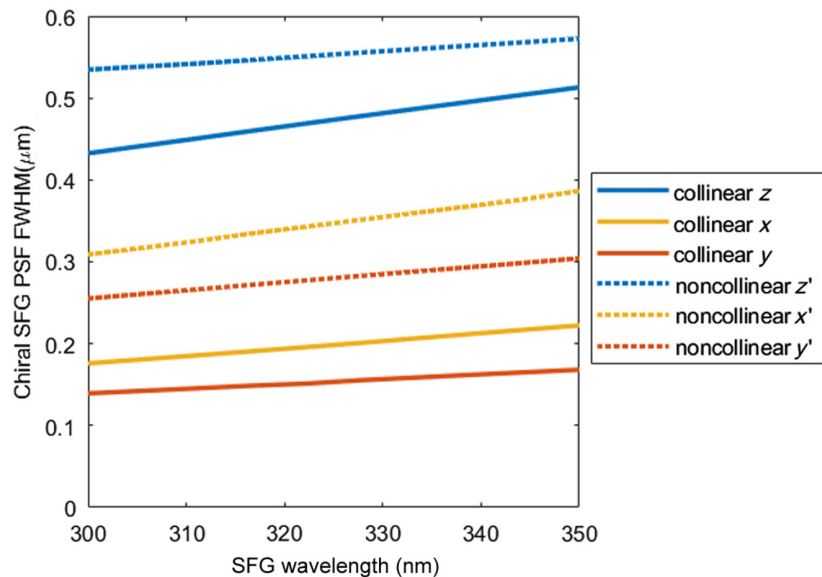


Fig. 3 Dependence of the chiral SFG PSF FWHM on wavelength. The wavelength of visible beam is tuned to scan the SFG wavelength across a typical electronic resonance range.

3.3 Experimental Setup

The light path is shown in Fig. 5(a). The Ti:sapphire oscillator (Spectra-Physics, MaiTai) generates 820 nm, 80 MHz, and 80 fs pulses for the IR pump beam. The accompanying optical parametric oscillator (OPO, Spectra-Physics Inspire 100) generates

520 nm pulses for the visible pump beam. Therefore, the wavelength of the chiral SFG signal was 318.2 nm. Note that due to the short wavelength, a special ultraviolet objective with an NA of 0.5 was used to collect the generated SFG signal. Both pump beams were collimated and expanded to a diameter of 10 mm to fully utilize the NA of the excitation objective. The 520 nm

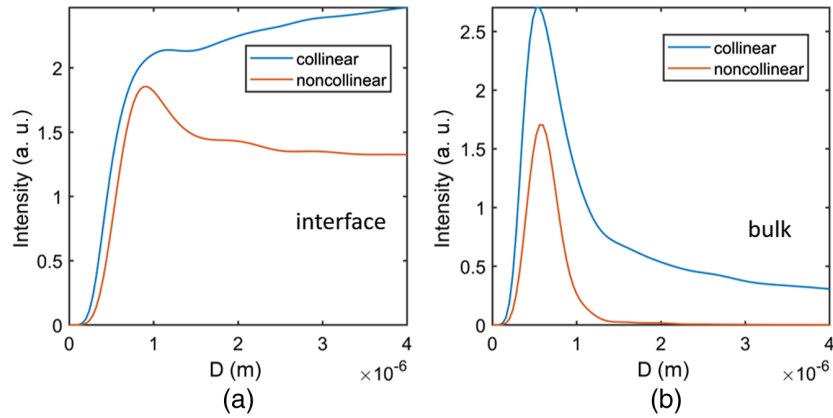


Fig. 4 Dependence of a far-field chiral SFG signal on the sample size. (a) Focusing on the interface between a chiral liquid and an achiral medium. (b) Focusing inside the bulk of a uniform chiral liquid.

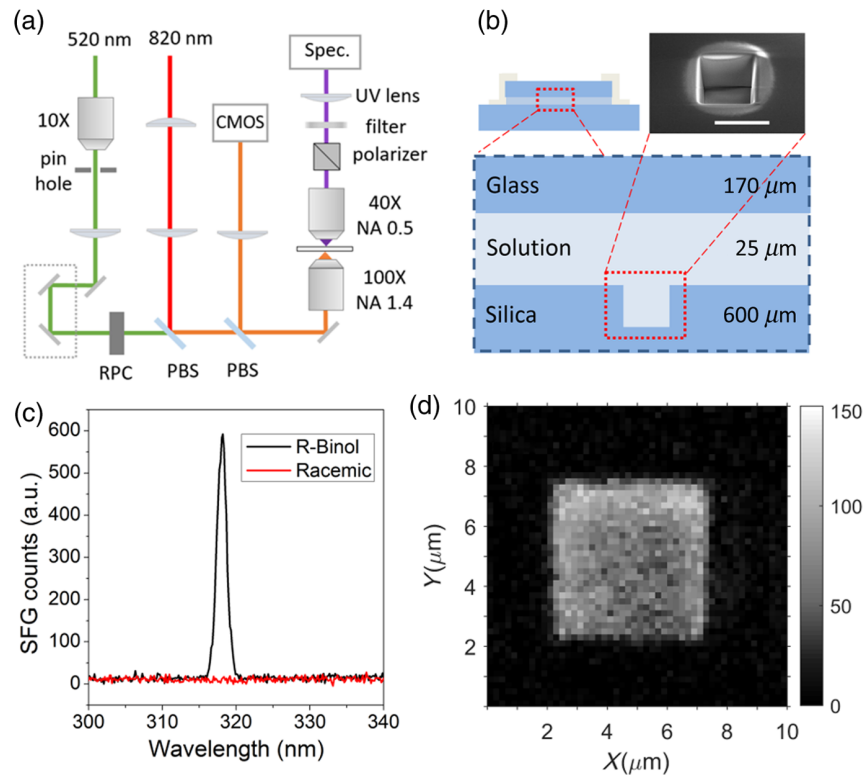


Fig. 5 Spectroscopic and imaging demonstration. (a) Experimental light path, where RPC denotes the radial polarization converter, PBS denotes the pellicle beam splitter, and Spec. denotes spectrometer with a liquid-nitrogen-cooled camera. (b) SEM image of the cubic liquid cell, with a scale bar of $5 \mu\text{m}$. (c) Spectral profile of the SFG signal from R-BINOL solution and a racemic mixture. (d) Collinear chiral SFG image of the cubic liquid cell.

beam was converted into an RP beam by a radial polarization converter (ARCOptix) and combined with the x -polarized 820 nm beam collinearly using an uncoated pellicle beam splitter (Thorlabs, BP208). An optical delay line in the RP beam path was used to finely adjust the temporal overlapping of the two beams. The combined collinearly propagating beam was directed into a homemade transmission-type microscope with a 1.4 NA focusing objective (Olympus, UPlanSApo 100XO) and a 0.5 NA

collecting objective, as mentioned earlier (Thorlabs, LMU-40X-UVB). The generated chiral SFG signal passed through two filters (Thorlabs, FGVU11-UV; Chroma, ET313/25BP) and a polarizer (Thorlabs, GLB10-UV) before being coupled into a spectrometer equipped with a liquid-nitrogen-cooled camera (Princeton Instrument, SP-2500, LN/400BR).

For spectroscopic and imaging demonstration, a $5\text{-}\mu\text{m}$ -long cubic liquid cell was prepared on the surface of a fused silica

slide by ion beam lithography, as shown in Fig. 5(b). The cell was filled with a 0.9 mol/L chiral R-BINOL solution, creating a chiral liquid cube in an achiral environment. The generated sum-frequency signal at 318.2 nm coincides with the electronic resonance of the BINOL molecule, which resulted in a significant signal enhancement.²² The two pump beams were collinearly focused into the liquid cell through the microscope, with an average power of 7 mW at 820 nm and 0.5 mW at 520 nm. To reduce the two-photon excitation of fluorescence background from BINOL molecules, a lower-power 520 nm beam was used. Fluorescence above 325 nm will be blocked by the filter.

3.4 Spectroscopic and Imaging Demonstration

By tightly focusing the RP and the x -polarized LP beams, the tensor element $\chi_{yxz}^{(2)}$ can be accessed by setting the detection polarizer in the y direction in the collinear modality. A typical spectral profile of the chiral SFG signal is shown in Fig. 5(c), where the peak wavelength matches the predicted value of 318.2 nm. Furthermore, when the sample was replaced by a racemic mixture of R-BINOL and S-BINOL solution with the same concentration, no signal was detected. Under the electric dipole approximation, it can be understood that $\chi_{yxz}^{(2)}$ for different enantiomers has opposite signs. Consequently, the induced nonlinear polarizations in the two enantiomers have a π phase difference, causing total destructive interference and hence a vanishing signal, as shown in Fig. 5(c). However, higher-order interactions may generate detectable chiral SFG signals, even in racemic mixtures.² Nevertheless, our spectroscopic measurement indicates that electric-quadrupole or magnetic-dipole contributions are negligible in the observed collinear chiral SFG signal. Therefore, the involvement of a localized longitudinal electric field does not alter the interaction or the selectivity of chiral SFG.

The microscopic imaging capability was demonstrated by raster scanning the sample using a piezo stage. The imaged plane was set at the lower liquid-glass interface, as shown in Fig. 5(b). The resulting image of the liquid cell is presented in Fig. 5(d), which agrees well with the scanning electron microscopy image in Fig. 5(b).

3.5 Resolution Characterization

To quantitatively characterize the spatial resolution, the transverse dimensions of the PSF of both collinear and noncollinear chiral SFG microscopy were measured using a knife-edge method.²³ The same chiral liquid cell as shown in Fig. 5(b) was used. For the noncollinear configuration, the two parallel pump beams were symmetrically displaced from the center of the objective lens by 1.6 mm, and both beams were p-polarized to facilitate an SPP polarization arrangement.¹⁴ Since chiral SFG only occurs in a chiral liquid, the interface between the chiral liquid and the cell wall can be considered equivalent to a knife edge for the chiral SFG characterizations. The interface was translated transversely across the focus within a range of 5 μm and at a 50 nm step. The generated chiral SFG intensity was recorded as a function of the interface positions, and the resulting distribution, shown in Fig. 6, represents the cumulative curve of the PSF with respect to the interface traveling distance along either the x or y direction.

To obtain the transverse dimensions of the PSF, numerical calculation based on the knife-edge method was performed

to fit the measured results. The intensity distributions used in the fitting were calculated by vectorial diffraction theory. Numerically fitted cumulative curves were obtained by using the least squares method according to experimental results, as plotted in Figs. 6(a), 6(b), 6(d), and 6(e) with the corresponding FWHM of the PSF marked in the figures. Then, the lower interface of the chiral liquid cell was used to characterize the longitudinal PSF for both the collinear and the noncollinear configurations. The lower interface will produce an enhanced signal due to the broken symmetry.¹² The measured FWHMs of the longitudinal PSF are displayed in Figs. 6(c) and 6(f). It should be noted that the imaging results were carried out in a region deep inside the chiral liquid cell. The refractive index mismatch between chiral liquid and glass-induced spherical aberration and distortion²⁴ results in a resolution lower than the theoretical limit for both the collinear and noncollinear schemes. Nevertheless, in comparison, the FWHM along the x , y , and z directions is 447, 471, 766 nm for collinear modality and 495, 672, 1124 nm for noncollinear modality, respectively. As shown in Fig. 6, a significant improvement of spatial resolution (~ 1.4 times) on the y and z directions can be observed.

4 Conclusion

In summary, we have demonstrated a new modality of chiral SFG microscopy. By employing tightly focused vectorial beams in a collinear excitation scheme, we can utilize the full aperture of the microscope, allowing for diffraction-limited spatial resolution. The enhanced resolution is confirmed by knife-edge measurements. Additional simulations demonstrate that this technique offers improved phase-matching conditions and exhibits strong prospects for application in vibrational resonance scenarios. These represent a significant improvement over the conventional noncollinear modality, which is constrained by the polarization restrictions imposed by the chiral nature of the interaction. The proposed technique enables label-free, chiral-selective SFG microscopy with high spatial resolution while also offering ease of integration with existing microscope modalities. This innovative approach has the potential to drive new developments for characterizing and spatially mapping chirality in biological and material systems.

Disclosures

The authors have no conflicts of interest to declare.

Code and Data Availability

All data and materials used in this study are available from the corresponding author upon reasonable request.

Acknowledgments

The authors thank Chuanshan Tian at Fudan University for fruitful discussions. This work was supported by the Guangdong Major Project of Basic and Applied Basic Research (Grant No. 2020B0301030009); the National Natural Science Foundation of China (Grant Nos. 91750203, 91850111, 11174019, 12004013, 92150301, and 61322509); the Ministry of Science and Technology of China [National Basic Research Program of China (Grant No. 2013CB921904)]; and the China Postdoctoral Science Foundation (Grant No. 2020M680220).

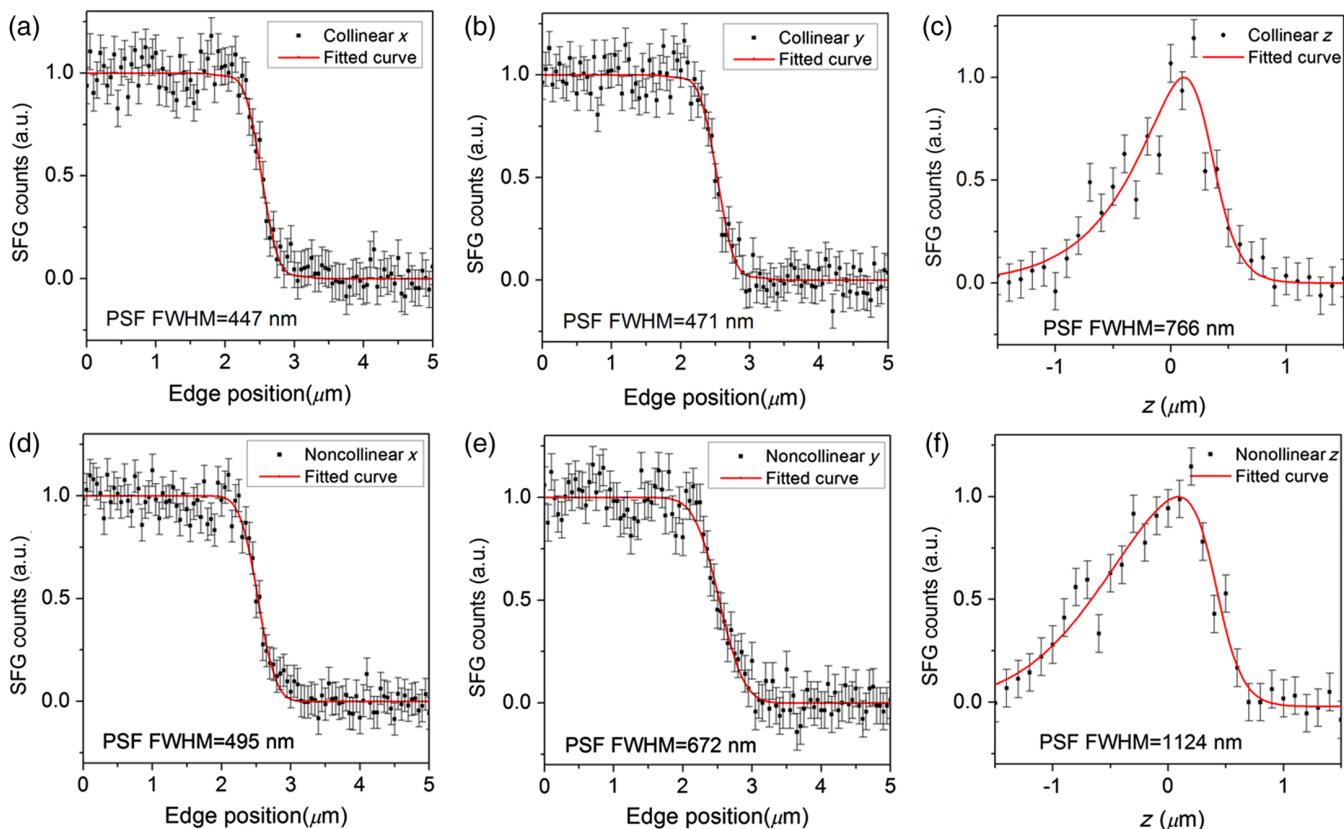


Fig. 6 Knife-edge measurement of the collinear and noncollinear configuration. The cumulative distribution of the PSF along the x , y , and z directions for collinear (a)–(c) and noncollinear (d)–(f) chiral SFG. The spatial resolutions of collinear chiral SFG along the y and z directions are enhanced by ~ 1.4 times, while the spatial resolutions along the x direction are comparable. The error bars represent the standard deviation.

References

- W. T. B. Kelvin, *The Molecular Tactics of a Crystal*, Clarendon Press (1894).
- Y. R. Shen, *Fundamentals of Sum-Frequency Spectroscopy*, Cambridge University Press (2016).
- M. A. Belkin et al., “Sum-frequency vibrational spectroscopy on chiral liquids: a novel technique to probe molecular chirality,” *Phys. Rev. Lett.* **85**, 4474 (2000).
- J. A. Giordmaine, “Nonlinear optical properties of liquids,” *Phys. Rev.* **138**, A1599 (1965).
- N. Ji et al., “Toward chiral sum-frequency spectroscopy,” *J. Am. Chem. Soc.* **128**, 8845–8848 (2006).
- S. Han et al., “Sum-frequency spectroscopy of electronic resonances on a chiral surface monolayer of bi-naphthol,” *Phys. Rev. B* **66**, 165415 (2005).
- M. A. Belkin et al., “Sum-frequency generation in chiral liquids near electronic resonance,” *Phys. Rev. Lett.* **87**, 113001 (2001).
- M. Belkin, Y. Shen, and R. Harris, “Sum-frequency vibrational spectroscopy of chiral liquids off and close to electronic resonance and the antisymmetric Raman tensor,” *J. Chem. Phys.* **120**, 10118–10126 (2004).
- L. M. Hupert and G. J. Simpson, “Chirality in nonlinear optics,” *Annu. Rev. Phys. Chem.* **60**, 345–365 (2009).
- Z. Wang et al., “Broad-bandwidth chiral sum frequency generation spectroscopy for probing the kinetics of proteins at interfaces,” *Langmuir* **31**, 11384 (2015).
- E. C. Yan et al., “Biological macromolecules at interfaces probed by chiral vibrational sum frequency generation spectroscopy,” *Chem. Rev.* **114**, 8471–8498 (2014).
- N. Ji et al., “Three-dimensional chiral imaging by sum-frequency generation,” *J. Am. Chem. Soc.* **128**, 3482–3483 (2006).
- K. Zhang et al., “Optically active sum frequency generation microscopy for cell imaging,” in *Int. Conf. Ultrafast Phenom.*, Optical Society of America, p. ThC3 (2006).
- G. Taupier et al., “Sum-frequency generation in sol-gel material doped with binaphthol,” *Appl. Phys. Lett.* **101**, 241911 (2012).
- V. Raghunathan et al., “Rapid vibrational imaging with sum frequency generation microscopy,” *Opt. Lett.* **36**, 3891–3893 (2011).
- A. Hanninen, M. W. Shu, and E. O. Potma, “Hyperspectral imaging with laser-scanning sum-frequency generation microscopy,” *Biomed. Opt. Express* **8**, 4230–4242 (2017).
- N. I. Koroteev, V. A. Makarov, and S. N. Volkov, “Sum-frequency generation in the bulk of an isotropic gyrotropic medium with two collinear pump beams,” *Laser Phys.* **9**, 655–664 (1999).
- A. Forbes, M. de Oliveira, and M. R. Dennis, “Structured light,” *Nat. Photonics* **15**, 253–262 (2021).
- G. Bautista and M. Kauranen, “Vector-field nonlinear microscopy of nanostructures,” *ACS Photonics* **3**, 1351–1370 (2016).
- H. Rubinsztein-Dunlop et al., “Roadmap on structured light,” *J. Opt.* **19**, 013001 (2016).
- J. X. Cheng and X. S. Xie, “Green’s function formulation for third-harmonic generation microscopy,” *JOSA B* **19**, 1604–1610 (2002).

22. I. Hanazaki and H. Akimoto, "Optical rotatory power of 2, 2'-dihydroxy-1, 1'-binaphthyl and related compounds," *J. Am. Chem. Soc.* **94**, 4102–4106 (1972).
23. A. H. Firester, M. E. Heller, and P. Sheng, "Knife-edge scanning measurements of subwavelength focused light beams," *Appl. Opt.* **16**, 1971–1974 (1977).
24. C. K. Tung et al., "Effects of index-mismatch-induced spherical aberration on two-photon imaging in skin and tissue-like constructs," *Proc. SPIE* **4963**, 95–104 (2003).

Biographies of the authors are not available.